Petroleum Science 20 (2023) 199–211

Contents lists available at ScienceDirect

Petroleum Science

journal homepage: www.keaipublishing.com/en/journals/petroleum-science

Original Paper

Proper orthogonal decomposition based seismic source wavefield reconstruction for finite element reverse time migration

Wen-Zhuo Tan [a, c], Bang-Yu Wu [a, c, *], Rui Li [b, c], Bo Li [c]

[a] School of Mathematics and Statistics, Xi'an Jiaotong University, Xi'an, Shaanxi, 710049, China
[b] School of Mathematics and Statistics, Shaanxi Normal University, Xi'an, Shaanxi, 710062, China
[c] SNOPEC Key Laboratory of Geophysics, Nanjing, Jiangsu, 211103, China

ARTICLE INFO

Article history:
Received 20 December 2021
Received in revised form
4 June 2022
Accepted 9 August 2022
Available online 17 August 2022

Edited by Jie Hao

Keywords:
Reverse time migration
Seismic wavefield reconstruction
Finite element modeling
Proper orthogonal decomposition

ABSTRACT

The large storage requirement is a critical issue in cross-correlation imaging-condition based reverse time migration (RTM), because it requires the operation of the source and receiver wavefields at the same time. The boundary value method (BVM), based on the finite difference method (FDM), can be used to reconstruct the source wavefield in the reverse time propagation in the same way as the receiver wavefield, which can reduce the storage burden of the RTM data. Considering that the FDM cannot well handle models with discontinuous material properties and rough interfaces, we develop a source wavefield reconstruction strategy based on the finite element method (FEM), using proper orthogonal decomposition (POD) to enhance computational efficiency. In this method, we divide the whole time period into several segments, and construct the POD basis functions to get a reduced order model (ROM) for the source wavefield reconstruction in each segment. We show the corresponding quantitative analysis of the storage requirement of the POD-FEM. Numerical tests on the homogeneous model show the effectiveness of the proposed method, while the layered model and part of the Marmousi model tests indicate that the POD-FEM can keep an excellent balance between computational efficiency and memory usage compared with the full-stored method (FSM) and the BVM, and can be effectively applied in imaging.

1. Introduction

Seismic imaging (Claerbout and Doherty, 1972; Gazdag, 1978; Bleistein, 1987; Keho and Beydoun, 1988; Hill, 2001; Zhang et al., 2002, 2019; Yang et al., 2015; Yao and Jakubowicz, 2016; Jiang et al., 2021; Li and Qu, 2022) plays an important role in exploration geophysics. Among many imaging methods, RTM has a significant advantage in high accuracy imaging of complex subsurface structures (Hemon, 1978; Whitmore, 1983; Baysal et al., 1983; McMechan, 1983; Fei et al., 2015). RTM includes three main parts: the forward propagation of the source wavefield, the backward propagation of the receiver wavefield, and the imaging condition. Among them, the imaging condition is the key component which affects the quality of the ultimate imaging profile. The common imaging conditions include: the cross-correlation imaging condition(Claerbout, 1971; Zhang et al., 2002), the excitation-time imaging condition (Chang and McMechan, 1986), the excitation-amplitude imaging condition (Nguyen and McMechan, 2012; Gu et al., 2015), the excitation potential imaging condition (Gu et al., 2014) and the sparse cross-correlation imaging condition (Nguyen and Mcmechan, 2015). Using the cross-correlation condition is a popular way to achieve high resolution imaging results. However, it requires the multiplication of the source and receiver wavefield at the same moment, which means that the source wavefields at all time steps must be stored, and it will cause a great storage burden.

To mitigate the huge wavefield storage, one alternative is to reconstruct the source wavefield in reverse time. Among many reconstruction methods, the most direct way is to store the source wavefields at every k ($k > 1$) time step, and estimate intermediate source wavefields by interpolation as needed during the backward recursion (Dussaud et al., 2008). Sun and Fu (2013) propose a Nyquist approach and obtain a significant reduction of storage by compression. The initial value method (checkpointing method) is

* Corresponding author. School of Mathematics and Statistics, Xi'an Jiaotong University, Xi'an, Shaanxi, 710049, China.
E-mail addresses: twz234@stu.xjtu.edu.cn (W.-Z. Tan), bangyuwu@xjtu.edu.cn (B.-Y. Wu), liruixjtu@163.com (R. Li), libo.swty@sinopec.com (B. Li).

https://doi.org/10.1016/j.petsci.2022.08.007

another practical scheme (Griewank and Walther, 1997; Symes, 2007; Anderson et al., 2012; Yang et al., 2016), which stores the source wavefields at checkpoints as the initial conditions and subsequently initiates a recursive forward recomputation of the source wavefield. However, the computational redundancy of the checkpointing method decreases the calculation efficiency of RTM algorithms (Nguyen and McMechan, 2012).

Due to the time reversibility of the numerical calculation of the wave equation, the boundary value method (BVM) is another source wavefield reconstruction strategy which is widely used in RTM. The BVM uses the wavefields at the final two time steps and the corresponding boundary values or boundary conditions to reconstruct the source wavefield. The random boundary condition proposed by Clapp (2009) is one implementation of the BVM, and Li et al. (2020) subsequently make an improvement by introducing reversible attenuation, which can eliminate the artifacts brought by the random layers near boundaries. Additionally, it is also practical to reconstruct the source wavefield by single or multi-layer boundary values stored in the forward propagation of the source wavefield (Feng and Wang, 2011; Nguyen and McMechan, 2012; Tan and Huang, 2014; Liu et al., 2015).

These source wavefield reconstruction methods are primarily based on the finite difference method (FDM) (Kelly et al., 1976; Dablain, 1986). However, the FDM cannot well handle models with discontinuous material properties and rough interfaces because of the lack of flexibility and the difficulty of processing complicated boundary conditions like the Neumann or Robin boundary condition (Cho et al., 2018; Sotelo et al., 2020). Compared with FDM, the FEM approach allows flexible meshing, and can effectively process the complicated boundary conditions based on the variational principle. Therefore, there are potential advantages to developing the FEM-based RTM method (Cho and Gibson, 2019).

The main drawbacks of the traditional FEM are its huge computational cost for solving large linear equations and the memory requirements for storing the mass and stiffness matrices (Liu et al., 2014b; Jia et al., 2021). Hence, the compressed sparse row (CSR) method (Saad, 2003; Liu et al., 2013, 2014a) can be used to decrease the storage. Recently, the lumped mass technique (Richter, 1994; Meng and Fu, 2017) has been applied to accelerate the finite element modeling by replacing the consistent mass matrix with the diagonal lumped mass matrix based on the conservation of mass. The kernel matrices storage (KMS) method introduced by Liu et al. (2014b) effectively improves the efficiency, and its subsequent development makes it a good component for finite element modeling (Meng and Fu, 2017; Su et al., 2019). Although the above techniques for the FEM are effective, it is still challenging to simulate the seismic wave propagation by traditional FEM for a large model size.

The combination of the POD method and the FEM for partial differential equations can provide efficient means of generating a reduced order model (ROM), which can alleviate the computational load and has been successfully applied to many fields (Kunisch and Volkwein, 2002; Schmidthäusler et al., 2013; Zhu et al., 2016; Corrado et al., 2016; Lu et al., 2017). Specifically, Luo et al. (2012) introduce the POD method to solve the acoustic equation. In general, POD-FEM constructs the POD basis functions based on the solutions in a certain period of time $[0,t_{\max}]$, then derives the ROM of the original system to quickly recalculate the solutions in the time interval $[0,t_{\max}]$. Considering that we need the forward modeling before the source wavefield reconstruction, the combination of the POD method and the BVM could be practical to accelerate the process and achieve an efficient low memory FEM-based RTM.

The rest of this paper is organized as follows. First, we introduce the theory of the FEM-based RTM. Then, we present the detailed steps for constructing the POD basis functions and the algorithm of the POD-FEM based source wavefield reconstruction. We also present a quantitative analysis of the storage requirement of the proposed method. Numerical tests on the homogeneous model, the layered model and part of the Marmousi model are used to compare the accuracy, computational efficiency and storage of our method with the FSM and the BVM. Finally, we state our conclusions and discuss the potential application of the proposed method for 3D modeling.

2. Theory and method

2.1. Imaging condition

RTM is a popular method to obtain a high-resolution imaging profile of the subsurface structures based on the following source-normalized cross-correlation imaging condition (Claerbout, 1971; Liu et al., 2015):

$$I(x,z)=\sum_{\mathbf{x_s}}\frac{\int_0^{t_{\max}} p_s(x,z,t;\mathbf{x_s})p_r(x,z,t_{\max}-t;\mathbf{x_s})\mathrm{d}t}{\int_0^{t_{\max}} p_s(x,z,t;\mathbf{x_s})^2\mathrm{d}t}, \tag{1}$$

where $I(x,z)$ is the imaging profile, $p_s(x,z,t;\mathbf{x_s})$ and $p_r(x,z,t;\mathbf{x_s})$ are the source wavefield and the receiver wavefield excited by the source at the position $\mathbf{x_s}=(x_s,z_s)$ and the corresponding seismic gathers recorded on the surface, respectively.

The above wavefields can be computed by the following constant density acoustic equations:

$$\frac{\partial^2 p_s(x,z,t;\mathbf{x_s})}{\partial t^2}-v(x,z)^2\nabla^2 p_s(x,z,t;\mathbf{x_s})=f(t;\mathbf{x_s}), \tag{2}$$

$$\frac{\partial^2 p_r(x,z,t;\mathbf{x_s})}{\partial t^2}-v(x,z)^2\nabla^2 p_r(x,z,t;\mathbf{x_s})=g(t,\mathbf{x_r};\mathbf{x_s}), \tag{3}$$

where $v=v(x,z)$ is the velocity, $(x,z)\in\Omega$ means the modeling area, $f(t;\mathbf{x_s})$ is the source term at the position $\mathbf{x_s}$, $g(t,\mathbf{x_r};\mathbf{x_s})$ is the received seismic gathers excited by the source at the position $\mathbf{x_s}$ and $\mathbf{x_r}$ are the positions of the receivers.

From Eq. (1), the principle of RTM imaging can be interpreted as the cross-correlation of two wavefields at the same moment, one computed by the forward time recursion, and the other computed in reverse time (Feng and Wang, 2011; Sun and Fu, 2013).

2.2. Finite element modeling of the seismic wavefield

Considering the reflections caused by the artificial truncated boundary in modeling, we need to introduce an effective absorbing boundary condition in the process of solving Eq. (2) and Eq. (3). In this work, we use the split perfectly matched layer (SPML) absorbing boundary condition. We next present the detailed steps of using FEM to realize the forward propagation of the seismic source wavefield.

The constant density acoustic equation with SPML (Komatitsch and Tromp, 2003) can be written as

$$\begin{cases} \left(\frac{\partial}{\partial t}+d_x\right)^2 p_1(x,z,t) = v(x,z)^2\frac{\partial^2 p_s}{\partial x^2}+f(t;\mathbf{x_s}), \\ \left(\frac{\partial}{\partial t}+d_x\right)^3 p_2(x,z,t) = -v(x,z)^2\frac{\partial d_x}{\partial x}\frac{\partial p_s}{\partial x}, \\ \left(\frac{\partial}{\partial t}+d_z\right)^2 p_3(x,z,t) = v(x,z)^2\frac{\partial^2 p_s}{\partial z^2}, \\ \left(\frac{\partial}{\partial t}+d_z\right)^3 p_4(x,z,t) = -v(x,z)^2\frac{\partial d_z}{\partial z}\frac{\partial p_s}{\partial z}, \end{cases} \tag{4}$$

where p_1, p_2, p_3, p_4 are part of wavefield, $p_s(x,z,t) = p_1+p_2+p_3+p_4$, $(x, z) \in \Omega_s$ means the region including the PML area, $d_x = \frac{3v}{2L_x}\ln\left(\frac{1}{R}\right)\left(\frac{\bar{x}}{L_x}\right)$ and $d_z = \frac{3v}{2L_z}\ln\left(\frac{1}{R}\right)\left(\frac{\bar{z}}{L_z}\right)$ are the attenuation functions in the corresponding directions, $R = 1\times10^{-3}$, L_x and L_z are the thicknesses of the PML, and $\bar{x}$ and $\bar{z}$ are the distances from the PML area to the inner area in the corresponding directions.

For the 3rd-order time partial derivatives in Eq. (4), we introduce the intermediate variables to avoid the difficulty and instability of discretizing them directly:

$$\overline{p}_2 = \left(\frac{\partial}{\partial t}+d_x\right)p_2, \quad \overline{p}_4 = \left(\frac{\partial}{\partial t}+d_z\right)p_4.$$

Multiplying Eq. (4) by an arbitrary test function $q_s(x, y)$, and conducting partial integration, the weak form of Eq. (4) can be written as

$$\begin{cases} \int_{\Omega_s}\left(\frac{\partial}{\partial t}+d_x\right)^2 p_1 q_s \mathrm{d}x\mathrm{d}z + \int_{\Omega_s} v^2\frac{\partial p_s}{\partial x}\frac{\partial q_s}{\partial x}\mathrm{d}x\mathrm{d}z \\ \quad = \int_{\Omega_s} f(t;\mathbf{x_s})q_s\mathrm{d}x\mathrm{d}z, \\ \int_{\Omega_s}\left(\frac{\partial}{\partial t}+d_x\right)^2 \overline{p}_2 q_s\mathrm{d}x\mathrm{d}z + \int_{\Omega_s} v^2\frac{\partial d_x}{\partial x}\frac{\partial p_s}{\partial x}q_s\mathrm{d}x\mathrm{d}z = 0, \\ \int_{\Omega_s}\left(\frac{\partial}{\partial t}+d_x\right)p_2 q_s\mathrm{d}x\mathrm{d}z = \int_{\Omega_s}\overline{p}_2 q_s\mathrm{d}x\mathrm{d}z, \\ \int_{\Omega_s}\left(\frac{\partial}{\partial t}+d_z\right)^2 p_3 q_s\mathrm{d}x\mathrm{d}z + \int_{\Omega_s} v^2\frac{\partial p_s}{\partial z}\frac{\partial q_s}{\partial z}\mathrm{d}x\mathrm{d}z = 0, \\ \int_{\Omega_s}\left(\frac{\partial}{\partial t}+d_z\right)^2 \overline{p}_4 q_s\mathrm{d}x\mathrm{d}z + \int_{\Omega_s} v^2\frac{\partial d_z}{\partial z}\frac{\partial p_s}{\partial z}q_s\mathrm{d}x\mathrm{d}z = 0, \\ \int_{\Omega_s}\left(\frac{\partial}{\partial t}+d_z\right)p_4 q_s\mathrm{d}x\mathrm{d}z = \int_{\Omega_s}\overline{p}_4 q_s\mathrm{d}x\mathrm{d}z. \end{cases} \tag{5}$$

When the N_s-dimensional finite element space $H_{h,s}$ is used to approximate the Soblev space $H_0^1(\Omega_s)$, we can use $p_{s,h}(x,z,t) = \sum_{i=1}^{N_s} P_s(i,t)\varphi_i(x,z)$ to approximate the source wavefield $p_s(x,z,t)$, where $P_s(i,t) = P_1(i,t)+P_2(i,t)+P_3(i,t)+P_4(i,t)$, and $\{\varphi_i(x,z)\}_{i=1}^{N_s}$ are the basis functions of $H_{h,s}$.

Let $P_s(t) = [P_s(1,t) \quad P_s(2,t) \quad \cdots \quad P_s(N_s,t)]^T$, then $P_s(t) = P_1(t)+P_2(t)+P_3(t)+P_4(t)$. Substituting $p_{s,h}$ into Eq. (5), we can get the finite element equations:

$$\begin{cases} M_1\frac{d^2P_1(t)}{dt^2}+2M_2\frac{dP_1(t)}{dt}+M_3P_1(t)+K_1P_s(t) = F_s(t), \\ M_1\frac{d^2\overline{P_2}(t)}{dt^2}+2M_2\frac{d\overline{P_2}(t)}{dt}+M_3\overline{P_2}(t)+K_xP_s(t) = 0, \\ M_1\frac{dP_2(t)}{dt}+M_2P_2(t)-M_1\overline{P_2}(t) = 0, \\ M_1\frac{d^2P_3(t)}{dt^2}+2M_4\frac{dP_3(t)}{dt}+M_5P_3(t)+K_2P_s(t) = 0, \\ M_1\frac{d^2\overline{P_4}(t)}{dt^2}+2M_4\frac{d\overline{P_4}(t)}{dt}+M_5\overline{P_4}(t)+K_zP_s(t) = 0, \\ M_1\frac{dP_4(t)}{dt}+M_4P_4(t)-M_1\overline{P_4}(t) = 0. \end{cases} \tag{6}$$

Let $\mathbf{N_s} = [\varphi_1 \quad \varphi_2 \quad \cdots \quad \varphi_{N_s}]^T$, we have

$$M_1 = \int_{\Omega_s}\mathbf{N_s}\mathbf{N_s}^T\mathrm{d}x\mathrm{d}z,$$

$$M_2 = \int_{\Omega_s} d_x\mathbf{N_s}\mathbf{N_s}^T\mathrm{d}x\mathrm{d}z,$$

$$M_3 = \int_{\Omega_s} d_x^2\mathbf{N_s}\mathbf{N_s}^T\mathrm{d}x\mathrm{d}z,$$

$$K_1 = \int_{\Omega_s} v^2\frac{\partial\mathbf{N_s}}{\partial x}\left(\frac{\partial\mathbf{N_s}}{\partial x}\right)^T\mathrm{d}x\mathrm{d}z,$$

$$K_x = \int_{\Omega_s} v^2\frac{\partial d_x}{\partial x}\left(\frac{\partial\mathbf{N_s}}{\partial x}\right)\mathbf{N_s}^T\mathrm{d}x\mathrm{d}z,$$

$$M_4 = \int_{\Omega_s} d_z\mathbf{N_s}\mathbf{N_s}^T\mathrm{d}x\mathrm{d}z,$$

$$M_5 = \int_{\Omega_s} d_z^2\mathbf{N_s}\mathbf{N_s}^T\mathrm{d}x\mathrm{d}z,$$

$$K_2 = \int_{\Omega_s} v^2\frac{\partial\mathbf{N_s}}{\partial z}\left(\frac{\partial\mathbf{N_s}}{\partial z}\right)^T\mathrm{d}x\mathrm{d}z,$$

$$K_z = \int_{\Omega_s} v^2\frac{\partial d_z}{\partial z}\left(\frac{\partial\mathbf{N_s}}{\partial z}\right)\mathbf{N_s}^T\mathrm{d}x\mathrm{d}z,$$

$$F_s(t;\mathbf{x_s}) = \int_{\Omega_s} f(t;\mathbf{x_s})\mathbf{N_s}\mathrm{d}x\mathrm{d}z.$$

In this modeling scheme, we compute the element mass and stiffness matrices first, then assemble them into the overall mass and stiffness matrices.

After discretizing the time derivatives in Eq. (6) with the second-order central difference method, we can calculate the source wavefield at different times $t_j = j\Delta t$, $j = 0, 1, \ldots, J$ by solving the following linear equations:

$$
\begin{cases}
(M_1+\Delta tM_2)P_1^{j+1}=(2M_1-\Delta t^2M_3)P_1^j \\
+(\Delta tM_2-M_1)P_1^{j-1}-\Delta t^2K_1P_s^j+\Delta t^2F_s^j, \\
(M_1+\Delta tM_2)\overline{P}_2^{j+1}=(2M_1-\Delta t^2M_3)\overline{P}_2^j \\
+(\Delta tM_2-M_1)\overline{P}_2^{j-1}-\Delta t^2K_xP_s^j, \\
(2M_1+\Delta tM_2)P_2^{j+1}=(2M_1-\Delta tM_2)P_2^j \\
+\Delta tM_1(\overline{P}_2^{j+1}+\overline{P}_2^j), \\
(M_1+\Delta tM_4)P_3^{j+1}=(2M_1-\Delta t^2M_5)P_3^j \\
+(\Delta tM_4-M_1)P_1^{j-1}-\Delta t^2K_2P_s^j, \\
(M_1+\Delta tM_4)\overline{P}_4^{j+1}=(2M_1-\Delta t^2M_5)\overline{P}_4^j \\
+(\Delta tM_4-M_1)\overline{P}_4^{j-1}-\Delta t^2K_zP_s^j, \\
(2M_1+\Delta tM_4)P_4^{j+1}=(2M_1-\Delta tM_4)P_4^j \\
+\Delta tM_1(\overline{P}_4^{j+1}+\overline{P}_4^j), \\
P_s^j=P_1^j+P_2^j+P_3^j+P_4^j,
\end{cases} \tag{7}
$$

where $P_s^j = P_s(t_j)$. The corresponding mass and stiffness matrices in Eq. (7) are repeated for different shots revisiting the same model.

We can conduct the backward propagation of the receiver wavefield in the same way.

2.3. Seismic source wavefield reconstruction based on the BVM

The principle of the BVM-based source wavefield reconstruction is in fact solving a constant density acoustic equation with the inhomogeneous Dirichlet boundary condition in reverse time. This problem can be written as

$$
\begin{cases}
\dfrac{\partial^2 p_s(x,z,t;\mathbf{x_s})}{\partial t^2}-v(x,z)^2\nabla^2 p_s(x,z,t;\mathbf{x_s})=f(t;\mathbf{x_s}), \\
p_s(x,z,t_{\max})=p_{s_{t_{\max}}}(x,z), \\
p_s(x,z,t_{\max}-\Delta t)=p_{s_{t_{\max}-\Delta t}}(x,z), \\
p_s(x,z,t)|_{\partial\Omega}=p_{\partial\Omega}(x,z,t),
\end{cases} \tag{8}
$$

where $p_{s_{t_{\max}}}$ and $p_{s_{t_{\max}-\Delta t}}$ are the last two wavefield snapshots we stored in the forward propagation of the source wavefield, and $p_{\partial\Omega}$ is the inhomogeneous Dirichlet boundary condition that we obtain.

Multiplying Eq. (8) by an arbitrary test function $q(x,y)\in H_0^1(\Omega)$, and conducting partial integration, the weak form of Eq. (8) can be written as:

$$
\int_\Omega \frac{\partial^2 p_s}{\partial t^2}q\,\mathrm{d}x\mathrm{d}z+\int_\Omega v^2\nabla p_s\cdot\nabla q\,\mathrm{d}x\mathrm{d}z=\int_\Omega f(t;\mathbf{x_s})q\,\mathrm{d}x\mathrm{d}z. \tag{9}
$$

To solve Eq. (9), we use the N-dimensional finite element space H_h to approximate the Soblev space $H_0^1(\Omega)$; then, $p_{s,h}(x,y,t)=\sum_{i=1}^N P_{s,h}(i,t)\varphi_i(x,z)$ can be used to approximate the reconstructed source wavefield $p_s(x,z,t)$.

Let

$$
P_{s,h}(t)=[P_{s,h}(1,t)\quad P_{s,h}(2,t)\quad\cdots\quad P_{s,h}(N,t)]^T,
$$
$$
\mathbf{N}=[\varphi_1\quad\varphi_2\quad\cdots\quad\varphi_N]^T.
$$

Then, we can derive the finite element equations from Eq. (9):

$$
M\frac{d^2P_{s,h}(t)}{dt^2}+KP_{s,h}(t)=F(t), \tag{10}
$$

where

$$
M=\int_\Omega \mathbf{N}\mathbf{N}^T\mathrm{d}x\mathrm{d}z,
$$
$$
K=\int_\Omega v^2\left[\frac{\partial\mathbf{N}}{\partial x}\left(\frac{\partial\mathbf{N}}{\partial x}\right)^T+\frac{\partial\mathbf{N}}{\partial z}\left(\frac{\partial\mathbf{N}}{\partial z}\right)^T\right]\mathrm{d}x\mathrm{d}z,
$$
$$
F(t)=\int_\Omega f(t;\mathbf{x_s})\mathbf{N}\mathrm{d}x\mathrm{d}z.
$$

After discretizing Eq. (10) by the central differencing method, we can realize the reconstruction of the source wavefield by solving the following linear equations in reverse time:

$$
\begin{aligned}
MP_{s,h}^{j-1}&=(2M-\Delta t^2K)P_{s,h}^j-MP_{s,h}^{j+1}+\Delta t^2F^j, \\
&j=J,J-1,\ldots,0,
\end{aligned} \tag{11}
$$

where $P_{s,h}^j=P_{s,h}(j\Delta t)$ and $F^j=F(j\Delta t)$.

The application of the inhomogeneous Dirichlet boundary condition can be realized by modifying the mass matrix M and the right-hand term.

Considering the huge computational cost of solving the large-scale linear Eqs. (7) and (11), we use the lumped mass technology to accelerate the calculation of the forward modeling and the BVM-based source wavefield reconstruction. In this way, the diagonal mass matrix M_d is used to replace the consistent mass matrix M, where (Liu et al., 2014a; Meng and Fu, 2017)

$$
M_d(i,j)=\delta_{i,j}M(i,j)\left(\sum_i\sum_j M(i,j)\right)\Big/\left(\sum_i M(i,i)\right).
$$

2.4. Seismic source wavefield reconstruction based on the POD-FEM

Solving Eq. (10) will be repeated many times in the process of RTM, so we further accelerate the calculation of finite element equations by the POD method to improve the efficiency of RTM.

The principle of the POD-FEM can be expressed as finding a new l dimensional finite element space H_l to approximate the Soblev space $H_0^1(\Omega)$. Therefore, the construction of the basis functions $\{\psi_i\}_{i=1}^l$ of H_l is the key point.

We first transform Eq. (8) into the constant density acoustic equation with the homogeneous Dirichlet boundary condition:

$$
\begin{cases}
\dfrac{\partial^2 p(x,z,t;\mathbf{x_s})}{\partial t^2}-v(x,z)^2\nabla^2 p(x,z,t;\mathbf{x_s})=h(x,z,t;\mathbf{x_s}), \\
p(x,z,t_{\max})=\widehat{p}_{s_{t_{\max}}}(x,z), \\
p(x,z,t_{\max}-\Delta t)=\widehat{p}_{s_{t_{\max}-\Delta t}}(x,z), \\
p(x,z,t)|_{\partial\Omega}=0,
\end{cases} \tag{12}
$$

where $p(x,z,t)=p_s(x,z,t)-p_{\partial\Omega}(x,z,t)$ means the modified source

wavefield, $h(x,z,t)=f(t)-\frac{\partial^2 p_{\partial\Omega}}{\partial t^2}+v^2\nabla^2 p_{\partial\Omega}$ is the modified source term, and $\hat{p}_{s_{t_{\max}}}(x,z)$ and $\hat{p}_{s_{t_{\max}-\Delta t}}(x,z)$ are the corresponding initial conditions whose boundary value are zeros.

In the forward computation of Eq. (2), we can get the source wavefields $p_s^j(x,z)=P_{s,h}^{j\ T}\mathbf{N}$ at the moment $t_j=j\Delta t, j=0,1,\ldots,J$. By extracting L snapshots from the above source wavefields at a fixed sampling interval Δt_{record}, we obtain a snapshot matrix $\mathbf{P_s}=[P_{s,h}^{w_1}\quad P_{s,h}^{w_2}\quad\cdots\quad P_{s,h}^{w_L}]$, where $w_1, w_2, \ldots, w_L$ are the index numbers. Then, by assigning zero to the boundary value, the discretized wavefield $p(x,z,t)$ can be expressed as

$$[p(t_{w_1})\quad p(t_{w_2})\quad\cdots\quad p(t_{w_L})]^T=\mathbf{P}^T\mathbf{N}(x,z), \tag{13}$$

where $t_{w_i}=w_i\Delta t, i=1,2,\ldots,L$ and $\mathbf{P}$ is the snapshot matrix obtained after assigning zero to $\mathbf{P_s}$.

According to the Nyquist sampling theorem, the sampling frequency must be greater than double the highest frequency of the original signal for complete reconstruction. Fig. 1a and b shows the Ricker wavelet with 15 Hz dominant frequency in the time domain and the corresponding frequency spectrum. Since the spectrum range of the Ricker wavelet with f_0 Hz dominant frequency is $[0, f_T](f_T=3f_0)$, the snapshot matrix $\mathbf{P}$ can be used to represent the solution of Eq. (12) in the time interval $[0, J\Delta t]$ when the sampling frequency $f_s\geq f_N=6f_0$. In the section of numerical experiments, we will show the effect of different f_s on the proposed algorithm.

By SVD, $\mathbf{P}=W\Sigma V^T, W\in\mathbf{R}^{N\times r}, \Sigma\in\mathbf{R}^{r\times r}, V\in\mathbf{R}^{L\times r}$ and $r=rank(\mathbf{P})$. The diagonal elements of $\Sigma(\sigma_1, \sigma_2, \ldots, \sigma_r)$ are singular values of $\mathbf{P}$, and we assume that $\sigma_1\geq\sigma_2\geq\cdots\geq\sigma_r>0$. The matrices W and V satisfy $W^TW=V^TV=I_r$, where I_r is the unit matrix.

In this way, an orthogonal basis of H_l can be expressed as $\{\psi_i=W(:,i)^T\mathbf{N}\}_{i=1}^{l}$ (Luo et al., 2012; Zhu et al., 2016; Corrado et al., 2016), where $W(:,i)$ means the i-th column vector of the matrix W, and l is the order of the ROM.

Then, $p_l(x,z,t)=\sum_{i=1}^{l}P_l(i,t)\psi_i(x,z)$ can be used to approximate $p(x,z,t)$, and the solving of Eq. (12) can be rewritten as a new variational problem:

$$\begin{cases}\displaystyle\int_\Omega\frac{\partial^2 p_l}{\partial t^2}\bar{q}\,dxdz+\int_\Omega v^2\nabla p_l\cdot\nabla\bar{q}\,dxdz\\ \quad=\displaystyle\int_\Omega h(x,z,t;\mathbf{x_s})\bar{q}\,dxdz,\quad\forall\bar{q}\in H_l,\\ p_l(x,z,t_{max})=\hat{p}_{s_{t_{max}}}(x,z),\\ p_l(x,z,t_{max}-\Delta t)=\hat{p}_{s_{t_{max}-\Delta t}}(x,z),\\ p_l(x,z,t)|_{\partial\Omega}=0.\end{cases} \tag{14}$$

Let

$$\mathbf{N}_\psi=[\psi_1\quad\psi_2\quad\cdots\quad\psi_l]^T,\quad\overline{W}=W(:,1:l),$$
$$P_{s,l}=[P_l(1,t)\quad P_l(2,t)\quad\cdots\quad P_l(l,t)]^T,$$

we can get the $l-$order ROM:

$$\overline{M}\frac{d^2P_{s,l}(t)}{dt^2}+\overline{K}P_{s,l}(t)=\overline{F}(t), \tag{15}$$

where

$$\overline{M}=\int_\Omega\mathbf{N}_\psi\mathbf{N}_\psi^T dxdz=\overline{W}^TM\overline{W},$$
$$\overline{K}=\int_\Omega v^2\nabla\mathbf{N}_\psi\cdot\nabla\mathbf{N}_\psi^T dxdz=\overline{W}^TK\overline{W},$$
$$\overline{F}(t)=\int_\Omega h(x,z,t;\mathbf{x_s})\mathbf{N}_\psi dxdz.$$

Finally, we can realize the reconstruction of the source wavefield by discretizing Eq. (15) with the central differencing method:

$$\begin{aligned}\overline{M}P_{s,l}^{j-1}&=(2\overline{M}-\Delta t^2\overline{K})P_{s,l}^j-\overline{M}P_{s,l}^{j+1}+\Delta t^2\overline{F}^j,\\ p_{s,l}^j&=P_{s,l}^{j\ T}\mathbf{N}_\psi+p_{\partial\Omega}(x,y,j\Delta t),\\ j&=J,J-1,\ldots,0.\end{aligned} \tag{16}$$

The L^2-error between the POD-FEM solution $p_{s,l}(x,z,t)$ and the FEM solution $p_{s,h}(x,z,t)$ can be expressed as (Luo et al., 2012)

$$O\left(\Delta t\sum_{i=l+1}^{r}\sigma_i\right)^{1/2},$$

which indicates that the error between the POD-FEM reconstructed result and the forward computed result is determined only by the time interval and the singular values we choose.

Therefore, we can use the parameter

$$\zeta=\sum_{i=1}^{l}\sigma_i\Big/\sum_{i=1}^{r}\sigma_i\times 100\%, \tag{17}$$

to decide a proper order l.

Typically, ζ should be taken to 99% or higher (Bui-Thanh et al., 2004; Lu et al., 2019) to avoid significant error. When the number of snapshots L is small, we can directly set the l to L. However, with the increase of the modeling time, the size of the snapshot matrix $\mathbf{P}$ gets larger. At this point, setting l to L will cause a high-order ROM, while finding a proper order l by a complete SVD will cost substantial computational resources. In other words, both approaches will reduce the modeling efficiency. Therefore, we introduce a parameter Δ, and divide the time period $[0, t_{\max}]$ into Δ segments. In each segment, we only use the stored snapshots in the corresponding time period to construct the POD basis functions and apply the above algorithm to realize the source wavefield reconstruction. In this way, the order l can be fixed as $\lceil\frac{L}{\Delta}\rceil$. It can not only satisfy the demand of accuracy ($\zeta>99\%$), but also avoid the complete SVD of the snapshot matrix $\mathbf{P}$.

2.5. Storage analysis

In this section, we use quantitative analysis to compare the storage requirement for the source wavefield reconstruction between the FSM and the POD-FEM.

For triangle-element-based FEM modeling, the minimum side length of the triangle mesh is determined by

$$h=\frac{v_{\min}}{Gf_0},$$

where $v_{\min}$ is the minimum velocity of a given model and G is the assigned number of points per wavelength (NPPW) corresponding to the dominant frequency of the source wavelet.

On the other hand, the stability condition of FEM modeling can be expressed as

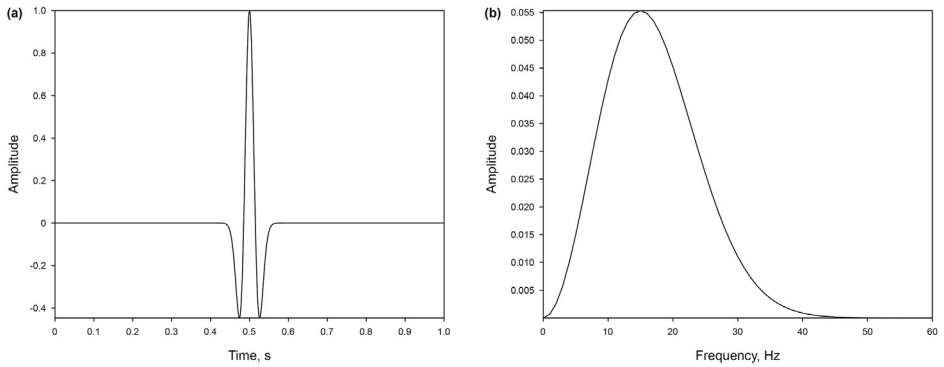

Fig. 1. (a) The Ricker wavelet with a dominant frequency of 15 Hz; (b) the frequency spectrum of (a).

$$\Delta t \le q\frac{h}{v_{\max}} = \frac{\alpha q}{G f_0},$$

where q is the courant number of the corresponding discrete form, $v_{\max}$ is the maximum velocity of a given model and $\alpha = v_{\min}/v_{\max}$.

Hence, we need to store

$$N_{\mathrm{FSM}} = \frac{t_{\max}}{\Delta t} \ge \frac{G f_0 t_{\max}}{\alpha q}$$

number of snapshots for the FSM.

As shown in our previous analysis, the sampling frequency for storing the source wavefields in POD-FEM modeling should be greater than $f_N = 6f_0$. Therefore, the sampling interval can be set as

$$\Delta t_{\mathrm{record}} = \frac{1}{f_N},$$

which means we only need to store

$$N_{\mathrm{POD}} = \frac{t_{\max}}{\Delta t_{\mathrm{record}}} = 6 f_0 t_{\max}$$

number of snapshots for the POD-FEM.

Table 1
The effect of ζ on the accuracy and CPU time of the POD-FEM with different orders.

Order	10	30	50	70	90
ζ	58.5952%	97.9118%	99.9527%	99.9983%	100%
Maximum error	72.8869%	9.1919%	1.1747%	0.0879%	0.0976%
CPU time	46.1706%	67.6482%	71.1876%	89.5290%	100%

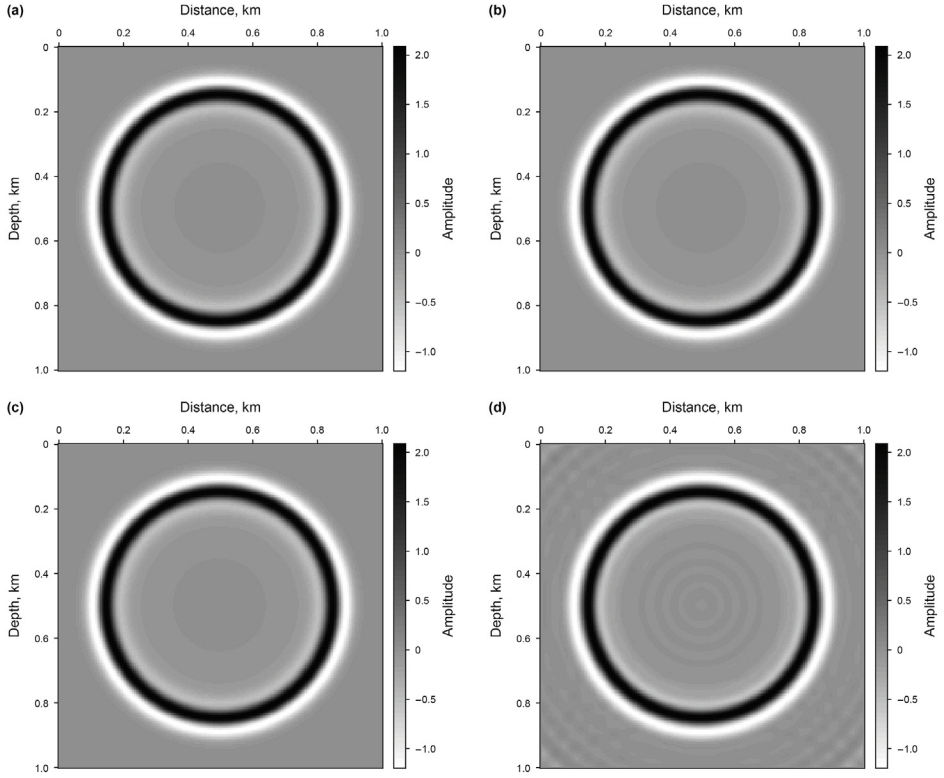

Fig. 2. (a) The forward computed source wavefield and the reconstructed source wavefield at 0.34 s for the homogeneous model computed by POD-FEM with different sampling frequencies: (b) 1000 Hz; (c) 90.9 Hz; (d) 62.5 Hz.

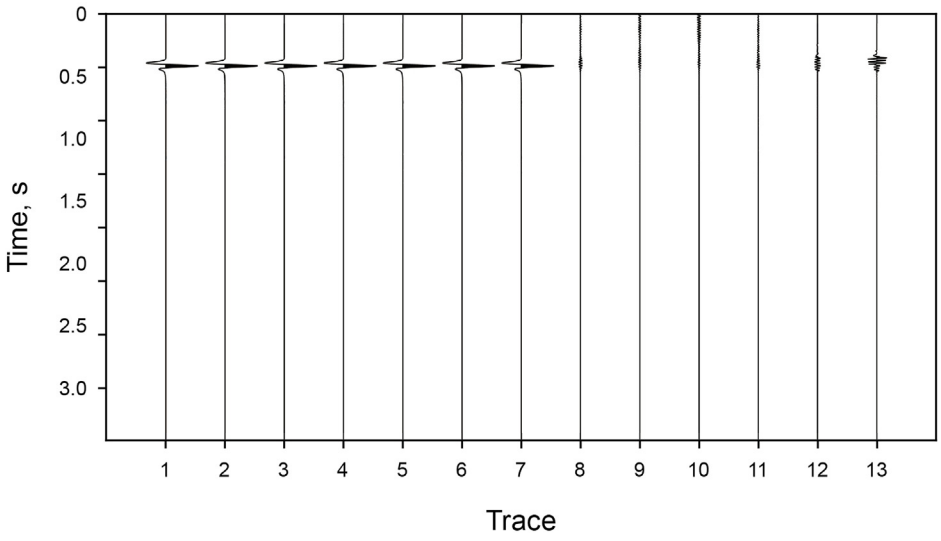

Fig. 3. The seismograms comparison between different methods recorded at (100 m, 100 m) for the homogeneous model. Trace 1 is the forward computed result, traces 2, 3, 4, 5, 6, and 7 are the reconstructed result computed by the POD-FEMs with Δ =1, 2, 4, 8, 16, and 32, respectively. Traces 8, 9, 10, 11, 12, and 13 are the differences ($\times 10^2$) between 2, 3, 4, 5, 6, 7, and 1, respectively.

Table 2
The effect of Δ on the accuracy and CPU time of the POD-FEM.

Δ	1	2	4	8	16	32
Maximum error	0.0791%	0.1155%	0.1019%	0.1173%	0.2953%	0.2421%
CPU time	100%	52.3565%	31.0642%	20.2954%	17.2010%	14.7286%

Hence, the ratio of the storage requirement between the FSM and the POD-FEM can be expressed as:

$$R = \frac{N_{\mathrm{FSM}}}{N_{\mathrm{POD}}} \geq \frac{G}{6\alpha q}.$$

In FEM modeling, the NPPW G for the P1 element should be greater than 19 to avoid significant numerical dispersion (Cao et al., 2015), and the courant number $q = 0.707107$ (Liu et al., 2014a).

Therefore,

$$R \geq \frac{4.48}{\alpha} \geq 4.48,$$

if we use the linear basis functions in modeling.

For higher-order basis functions, we can reduce the NPPW G, but the stability condition is more stringent, which means that the ratio R would still be significantly greater than 4.

In other words, our method can achieve more than 80% savings of memory compared with the FSM, and the reduction would be more significant for a model with larger velocity range.

3. Numerical experiments

In this section, we first carry out a test on the homogeneous model to verify the effect of the parameters f_s, ζ and Δ on the accuracy of the POD-FEM. Then, we use the layered model and part of the Marmousi model to compare the accuracy, memory usage and computational efficiency of our POD-FEM source wavefield reconstruction method with the FSM and the BVM. The calculation is done on the computing platform (Intel(R) Xeon(R) Silver 4216 CPU @ 2.10 GHz, 128 GB of memory, and MATLAB codes) and we use the second-order basis functions in the following test.

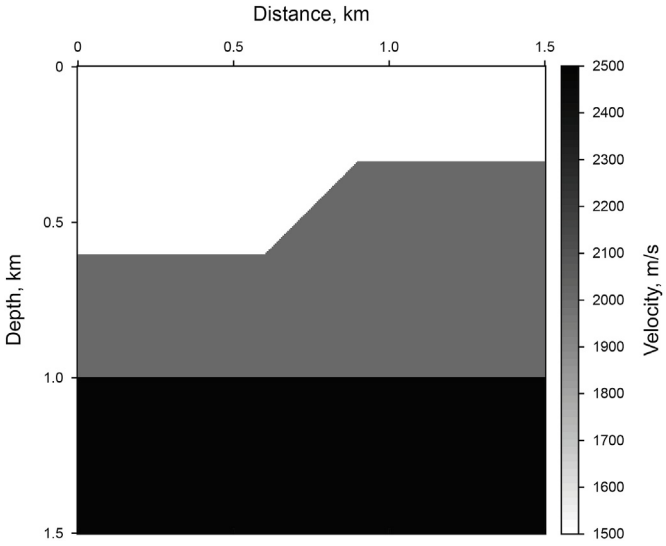

Fig. 4. Layered velocity model.

3.1. Homogeneous model

The size of the homogeneous model we use is 1000 m × 1000 m and the velocity is 1500 m/s. The Ricker wavelet with a dominant frequency of 15 Hz is placed at (x_s, z_s)=(500 m, 500 m). We discretize this model by triangular meshes, and then get 20000 elements and 40401 nodes.

The time increment is set to 1 ms and the maximum time is 1 s. We first test the effect of f_s on the accuracy of the POD-FEM. In the process of the forward computation, the thicknesses of the PML L_x and L_z are set as 200 m and we store the source wavefields every 1, 11, and 16 time steps, respectively. We fix the parameter Δ as 1 and the order l of the ROM as 90.

Fig. 2a shows the forward computed snapshot at 0.34 s, and Fig. 2b, c and d show the reconstructed wavefield at 0.34 s computed by POD-FEM with different sampling frequencies f_s, respectively. There is no significant difference between Fig. 2a, b

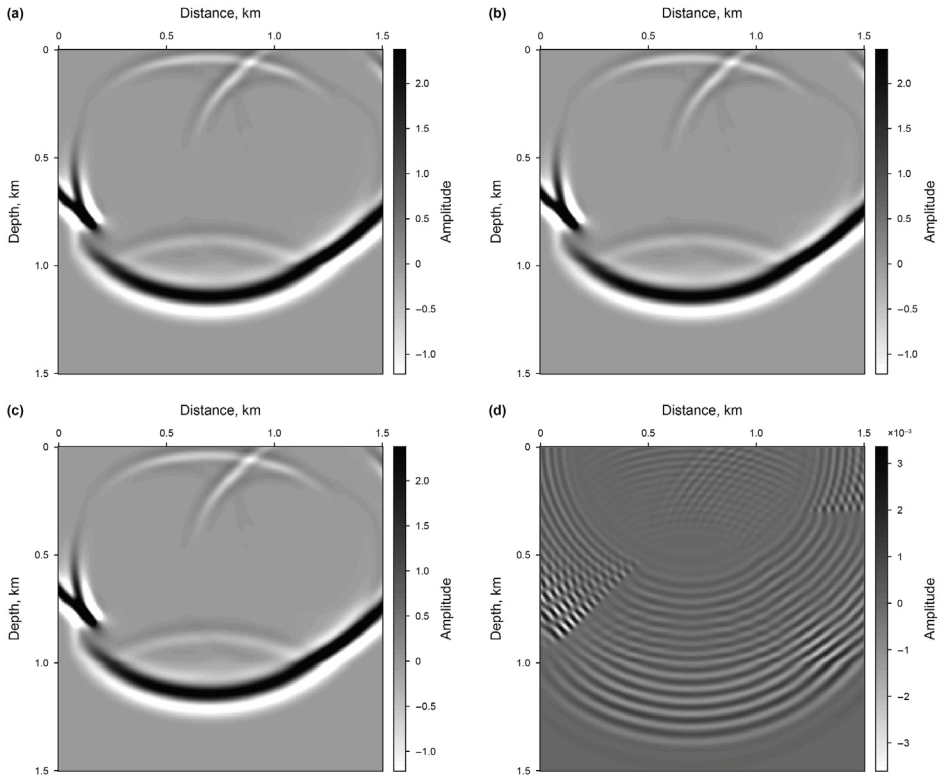

Fig. 5. The reconstructed source wavefield at 0.75 s for the layered model computed by (a) FSM; (b) BVM; (c) POD-FEM. (d) The difference between (a) and (c).

and c, while the obvious artifacts in Fig. 2d can be identified.

To give a quantitative comparison, we use

$$error = |p_s(x,z,t_j) - p_{\mathrm{re}}(x,z,t_j)| / \|p_s(x,z,t_j)\|_{L_\infty},$$

to measure the accuracy of the reconstructed wavefield at a fixed moment t_j, where $p_s(x, z, t_j)$ is the forward computed source wavefield and $p_{\mathrm{re}}(x, z, t_j)$ is the reconstructed source wavefield.

Table 3
Accuracy, CPU time and memory usage of different methods in Fig. 5.

Scheme	FSM	BVM	POD-FEM
Maximum error	0%	0%	0.1517%
CPU time	0%	100%	40.3686%
Memory	100%	1.9268%	10.9133%

The maximum error of the above POD-FEM results with sampling frequencies of 1000, 90.9 and 62.5 Hz are 0.0022%, 0.0976% and 10.5981% respectively, which indicates that the accuracy of the POD-FEM satisfies the requirements of practical applications when the sampling frequency $f_s \geq f_N$. Although the error of the POD-FEM decreases with the increase of f_s, we set f_s as f_N to save more storage.

We then test the effect of the order l on the maximum error and CPU time of the POD-FEM. The sampling frequency f_s is now fixed as 90 Hz, and we perform a complete SVD for the snapshot matrix $\mathbf{P}$ in this test to get the exact ζ for the ROM with different l. Table 1 shows the corresponding results. With the increase of l and ζ, the maximum error between the forward computed wavefield and the reconstructed source wavefield at 0.34 s is reduced significantly. Specifically, the error is acceptable when $\zeta > 99\%$. The CPU time is proportional to ζ, which means that the computational efficiency

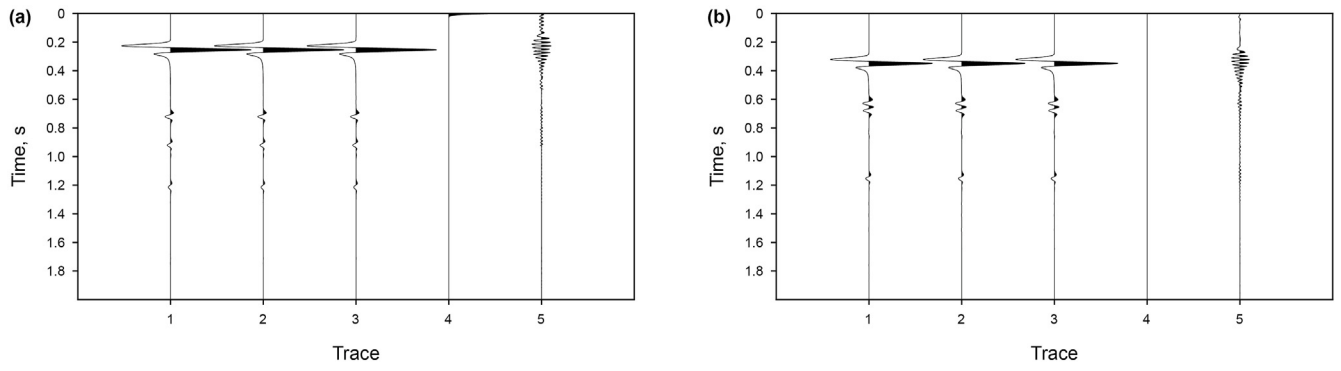

Fig. 6. The seismograms comparison between different methods recorded at (a) (500 m, 100 m) and (b) (1000 m, 200 m) for the layered model. Traces 1, 2, and 3 are the forward computed, BVM and POD-FEM results, respectively. Traces 4 and 5 are the differences ($\times 10^2$) between 2, 3, and 1.

will be affected if l is too large. Therefore, it is necessary to use the parameter Δ to avoid an excessively large order l.

To illustrate the effect of Δ, we choose different Δ for simulation. The maximum time is set to 4 s; the source term and the meshing are same as previous tests. Table 2 shows the accuracy and the CPU time of the modeling with different Δ, which indicates that, with the increase of the Δ, the maximum error between the forward computed wavefield and the reconstructed source wavefield at 0.34 s gets larger gradually. The CPU time reduces with the increase of Δ, but the reduction is getting smaller when $\Delta > 8$. This is mainly caused by the increasing magnitude of the SVD. Therefore, we can fix Δ as 8 to achieve high accuracy and efficiency in source wavefield reconstruction.

Fig. 3 displays the seismograms in time domain recorded at (100 m, 100 m) for the homogeneous model. Trace 1 is the forward computed result, while traces 2, 3, 4, 5, 6, and 7 are the reconstructed results computed by the POD-FEM with $\Delta = 1, 2, 4, 8, 16$, and 32, respectively. Traces 8, 9, 10, 11, 12, and 13 are the differences ($\times 10^2$) between 2, 3, 4, 5, 6, 7, and 1, respectively. With the increase of the Δ, the error of POD-FEM result also increases in the time domain, but there is no obvious error accumulation.

3.2. Layered model

We next perform the test on a layered model, which is shown in Fig. 4. The Ricker wavelet with a dominant frequency of 15 Hz is placed at (x_s, z_s)=(700 m, 0 m). After discretizing this model by the triangular mesh, we obtain 45000 elements and 90601 nodes. The time increment is set as 1 ms and the maximum time is 2 s. In the process of the forward computation, the thicknesses of the PML L_x and L_z are set as 300 m. We store the source wavefields every 11 time steps and store all the boundary values. The parameter Δ is fixed as 8, and the order l of the ROM is 23.

Fig. 5a, b and c show the reconstructed source wavefield at 0.75 s for this model computed by FSM, BVM and POD-FEM, respectively, while Fig. 5d shows the difference between Fig. 5a and c. There is no visible difference between these snapshots.

Table 3 shows the quantitative comparison of these methods for the layered model. With a 0.1517% error, the POD-FEM can save 89.0867% of memory compared with the FSM, which is consistent with our analysis. The CPU time of the POD-FEM is 40.3686% of that of the BVM, and it can be reduced further if we use the consistent mass matrix, since the application of the lumped mass technology avoids having to solve the large scale linear equations for the BVM.

Fig. 6a and b displays the seismograms in the time domain recorded at (500 m, 100 m) and (1000 m, 200 m), respectively. Traces 1, 2, and 3 are the forward computed, BVM and POD-FEM results, respectively. Traces 4 and 5 are the differences ($\times 10^2$) between 2, 3, and 1. Although the error of the POD-FEM is more obvious in the time domain compared with the BVM, it won't seriously impact the imaging results because the error is mainly in the direct wave.

To illustrate the effects of the POD-FEM for prestack RTM, we migrate the synthetic data computed for this layered model. We shot from 0 m to 1500 m on the surface with an interval of 100 m and in total get 16 shots. Receivers are spread on both sides of the shot point with an equal distance of 10 m. The source term and the time increment are the same as before. Fig. 7a and b displays the RTM results computed by the BVM and the POD-FEM respectively, while Fig. 7c is the difference between Fig. 7a and b. The RTM results show the subsurface structures of the layered model well, and the maximum error between Fig. 7a and b is 0.5523%, which indicates that our POD-FEM won't bring in additional artifacts.

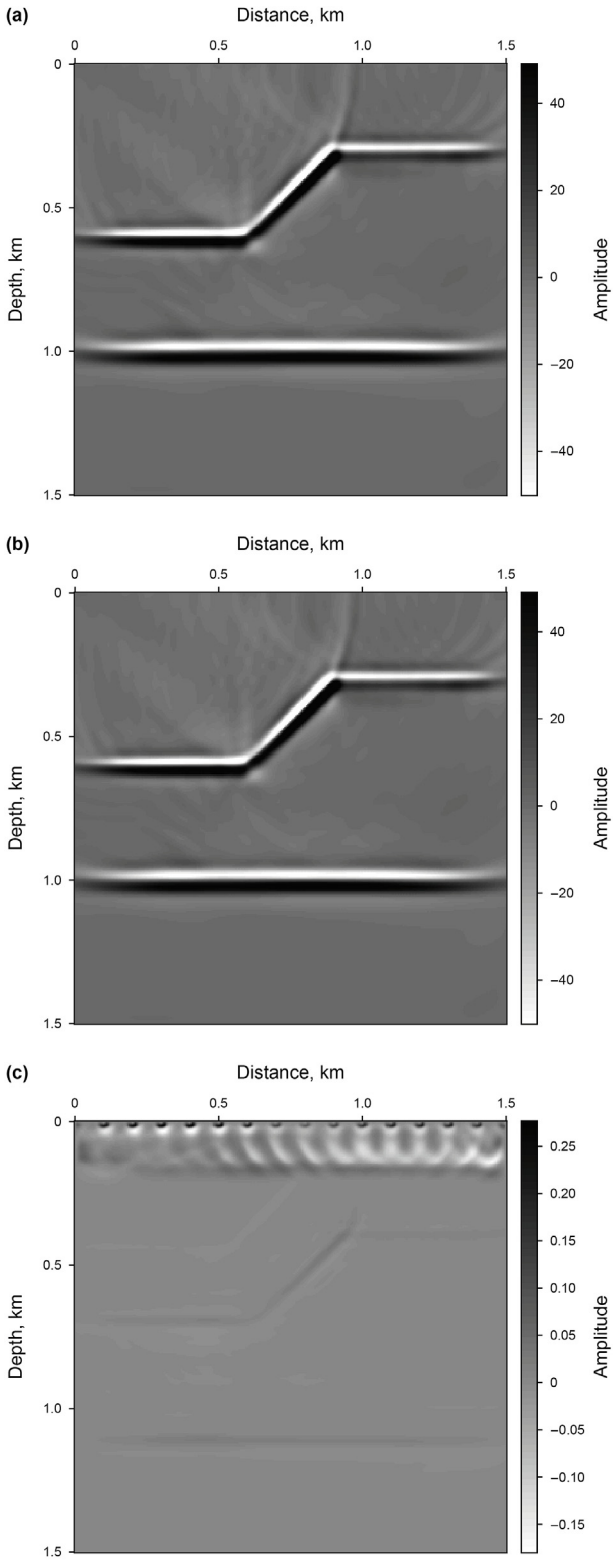

Fig. 7. The RTM results for the layered model computed by (a) BVM; (b) POD-FEM. (c) The difference between (a) and (b).

3.3. Marmousi model

Finally, we test on part of the Marmousi model to verify the effectiveness of the POD-FEM for a model with complex subsurface

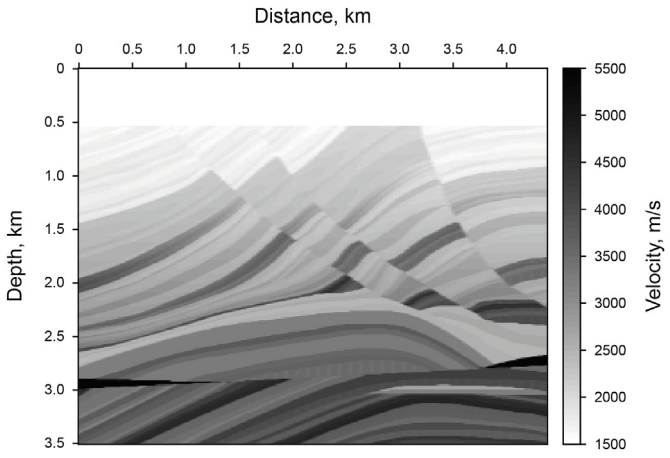

Fig. 8. Part of the Marmousi velocity model.

structures. In order to better mute the direct wave, we add some water layers. The model is shown in Fig. 8. We set the Ricker wavelet with a dominant frequency of 15 Hz at (x_s, z_s) =(2200 m, 0 m) as the source term. With the triangular mesh, we get 196000 elements and 393261 nodes. The time increment is set as 0.5 ms to obtain stable results and the maximum time is 3.5 s. In the process of the forward computation, the thicknesses of the PML L_x and L_z are set as 500 m. We store the source wavefields every 22 time steps and store all the boundary values. The parameter Δ is fixed as 8, and the order l of the ROM is 40.

Fig. 9a, b and c show the reconstructed source wavefield at 1.5 s for this model computed by FSM, BVM and POD-FEM, respectively, while Fig. 9d shows the difference between Fig. 9a and c. There is still no visible difference between these snapshots, which means that the accuracy of the POD-FEM is acceptable even on a complex model.

Table 4 shows the quantitative comparison of these methods for part of the Marmousi model. With a 0.1617% error, the POD-FEM

Table 4
Accuracy, CPU time and memory usage of different methods in Fig. 9.

Scheme	FSM	BVM	POD-FEM
Maximum error	0%	0%	0.1617%
CPU time	0%	100%	30.1619%
Memory	100%	0.6696%	5.1981%

can save 94.8019% of memory compared with the FSM. Compared with the layered model results, the memory saving of the POD-FEM is more notable due to the larger velocity range of part of the Marmousi model. The CPU time of the POD-FEM is 30.1619% of that of the BVM, which means that the improvement of the efficiency for the POD-FEM is more significant with the increase of the model size.

Fig. 10a and b displays the seismograms in the time domain recorded at (1000 m, 200 m) and (3000 m, 400 m), respectively. Traces 1, 2, and 3 are the forward computed, BVM, and POD-FEM results respectively. Traces 4 and 5 are the differences ($\times$ 10^2) between 2, 3, and 1. The waveforms between the forward and reconstructed results fit well and there is still no obvious error accumulation of our POD-FEM in the time domain for this complex model.

We then shot from 500 m to 3800 m on the surface with an interval of 100 m and in total get 34 shots. A total of 96 receivers are spread on both sides of the shot point with an equal distance of 25 m. The source term and the time increment are the same as previous tests. Fig. 11a and b displays the RTM results computed by the BVM and the POD-FEM respectively, while Fig. 11c shows the difference between Fig. 11a and b. There is good consistency between these two images, and the maximum error between Fig. 11a and b is 0.6218%. The above results show that our method can be applied effectively in imaging.

4. Discussion

This paper discusses the application of the POD-FEM for the

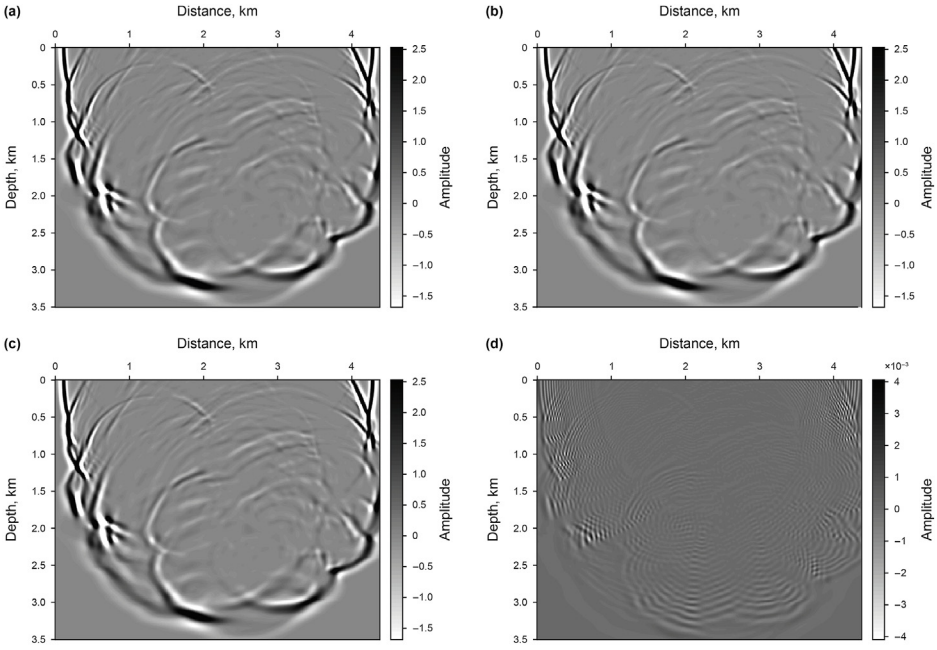

Fig. 9. The reconstructed source wavefield at 1.5 s for part of the Marmousi model computed by (a) FSM; (b) BVM; (c) POD-FEM. (d) The difference between (a) and (c).

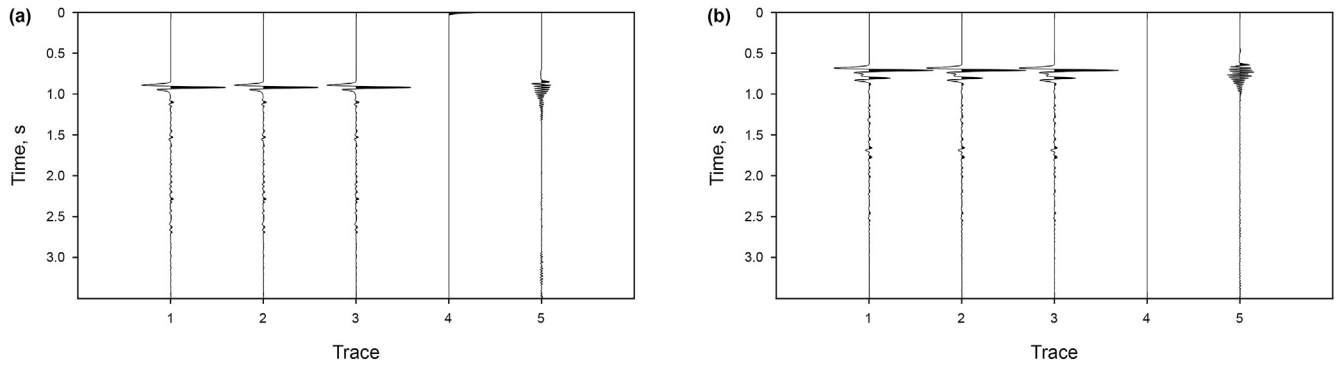

Fig. 10. The seismograms comparison between different methods recorded at (a) (1000 m, 200 m) and (b) (3000 m, 400 m) for part of the Marmousi model. Traces 1, 2, and 3 are the forward computed, BVM and POD-FEM results, respectively. Traces 4 and 5 are the differences ($\times 10^2$) between 2, 3, and 1.

reconstruction of the source wavefield in the process of 2D RTM. Considering that the application of the corresponding method for a 3D realistic model requires more values, and hence more resource costs, we discuss improvement in the possible reduction of storage and improvement of efficiency for a 3D situation. Compared with the 2D modeling, there is no additional computational strategy for the 3D POD-FEM. Thus, the ratio of the storage requirement between the FSM and the POD-FEM in 3D modeling can still be expressed as

$$R \geq \frac{G}{6\alpha q}.$$

Since the velocity range of the 3D realistic model would be sharper, and the courant number q would be more stringent for 3D modeling, the ratio R would be greater than it is in 2D modeling, which means one can save more storage.

From Eq. (11), the main calculation of the BVM is the multiplication between the matrix and the vector. Namely, if there are N nodes after the finite element discretization, the total computational cost for 3D BVM modeling is $O\left(2JN^2\right)$, where J is the total number of time steps. Then, the main calculation of the POD-FEM is the SVD, whose cost is about $O\left(4LN^2\right)$, and L is the number of the snapshots we extract in modeling. Considering that $L \approx \frac{J}{R}$, the main calculation cost of the POD-FEM is about $O\left(\frac{4}{R}JN^2\right)$. As we showed previously, the ratio R will be larger in 3D modeling. Therefore, we may achieve a more significant improvement of efficiency for 3D POD-FEM source wavefield reconstruction.

5. Conclusion

In this paper, we propose a POD-FEM based seismic source wavefield reconstruction method for RTM. We use a low-dimensional finite element space to approximate the Soblev space and construct the POD basis functions based on the SVD. After deriving the corresponding acoustic finite element equations, we provide a detailed algorithm for reconstructing the source wavefield by the POD-FEM. To further accelerate the computational efficiency of the POD-FEM, we introduce the parameter Δ to divide the whole time period into Δ segments, and construct a small number of POD basis functions to get a lower ROM in each segment. The numerical tests on the homogeneous model show that the sampling frequency f_s for storing the source wavefield can be set as the Nyquist frequency, while the parameter Δ can be set as 8. The numerical tests on the layered model and part of the Marmousi model show the excellent balance of our method between

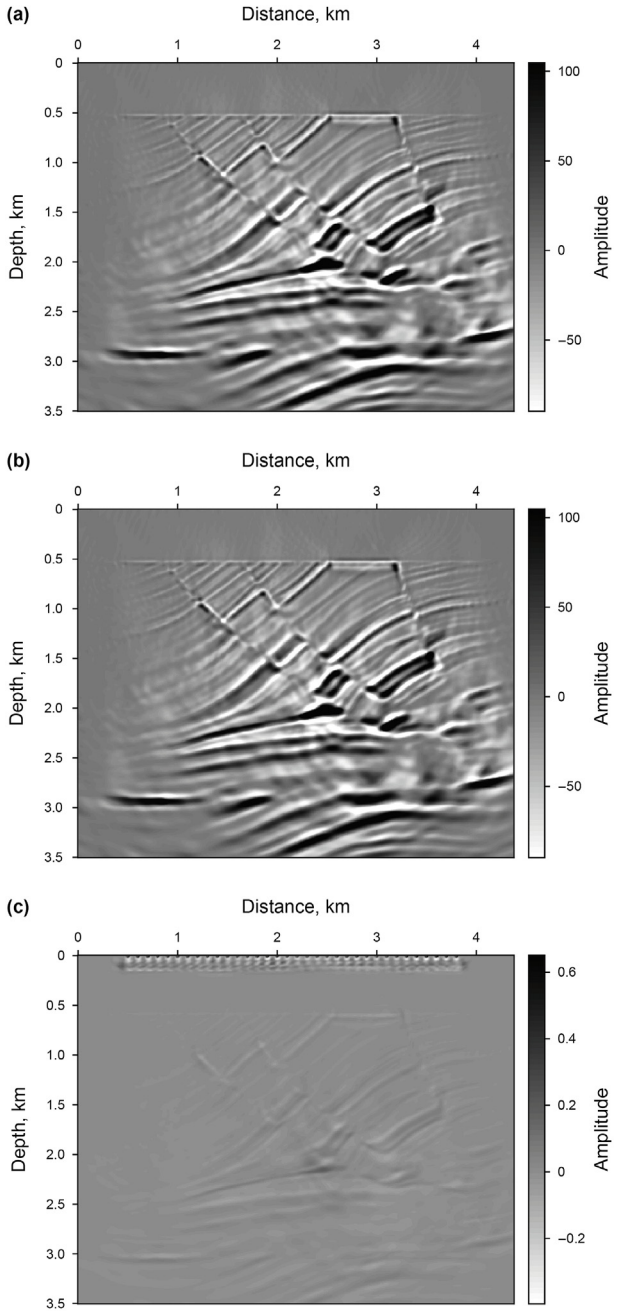

Fig. 11. The RTM results for part of the Marmousi model computed by (a) BVM; (b) POD-FEM. (c) The difference between (a) and (b).

computational efficiency and memory usage compared with the FSM and the BVM. Specifically, the RTM results indicate that the POD-FEM won't introduce additional artifacts and can be applied well in imaging. Our method can be generalized to other wave equations without further effort.

Acknowledgements

This work was supported by Natural Science Basic Research Program of Shaanxi (Program No. 2023-JC-YB-269) and the National Natural Science Foundation of China (Grant No. 41974122).

References

Anderson, J., Tan, L., Wang, D., 2012. Time-reversal checkpointing methods for RTM and FWI. Geophysics 77 (4), S93–S103. https://doi.org/10.1190/geo2011-0114.1.
Baysal, E., Kosloff, D., Sherwood, J., 1983. Reverse-time migration. Geophysics 48 (11), 1514–1524. https://doi.org/10.1190/1.1441434.
Bleistein, N., 1987. On the imaging of reflectors in the earth. Geophysics 52 (7), 931–942. https://doi.org/10.1190/1.1442363.
Bui-Thanh, T., Damodaran, M., Willcox, K., 2004. Aerodynamic data reconstruction and inverse design using proper orthogonal decomposition. AIAA J. 42 (8), 1505–1516. https://doi.org/10.2514/1.2159.
Cao, D., Zhou, J., Yin, X., 2015. The study for numerical dispersion and stability of wave motion with triangle-based finite element algorithm. Chin. J. Geophys. 58 (5), 1717–1730. http://www.geophy.cn//EN/abstract/article_11502.shtml.
Chang, W., McMechan, G.A., 1986. Reverse-time migration of offset vertical seismic profiling data using the excitation-time imaging condition. Geophysics 51 (1), 67–84. https://doi.org/10.1190/1.1442041.
Cho, Y., Gibson, J.R.L., 2019. Reverse time migration via frequency-adaptive multiscale spatial grids. Geophysics 84 (2), S41–S55. https://doi.org/10.1190/geo2018-0292.1.
Cho, Y., Gibson, J.R.L., Vasilyeva, M., et al., 2018. Generalized multiscale finite elements for simulation of elastic-wave propagation in fractured media. Geophysics 83 (1). https://doi.org/10.1190/geo2017-0076.1. WA9–WA20.
Claerbout, J.F., 1971. Toward a unified theory of reflector mapping. Geophysics 36 (3), 467–481. https://doi.org/10.1190/1.1440185.
Claerbout, J.F., Doherty, S.M., 1972. Downward continuation of moveout-corrected seismograms. Geophysics 37 (5), 741–768. https://doi.org/10.1190/1.1440298.
Clapp, R.G., 2009. Reverse Time Migration with Random Boundaries. SEG Technical Program Expanded Abstracts 2009. Society of Exploration Geophysicists, pp. 4338–4342. https://doi.org/10.1190/1.3255432.
Corrado, C., Lassoued, J., Mahjoub, M., et al., 2016. Stability analysis of the POD reduced order method for solving the bidomain model in cardiac electrophysiology. Math. Biosci. 272, 81–91. https://doi.org/10.1016/j.mbs.2015.12.005.
Dablain, M.A., 1986. The application of high-order differencing to the scalar wave equation. Geophysics 51 (1), 54–66. https://doi.org/10.1190/1.1442040.
Dussaud, E., Symes, W., Williamson, P., et al., 2008. Computational Strategies for Reverse-Time Migration. SEG Technical Program Expanded Abstracts 2008. Society of Exploration Geophysicists, pp. 3713–3717. https://doi.org/10.1190/1.3059336.
Fei, T., Luo, Y., Yang, J., et al., 2015. Removing false images in reverse time migration: the concept of de-primary. Geophysics 80 (6), S237–S244. https://doi.org/10.1190/geo2015-0289.1.
Feng, B., Wang, H., 2011. Reverse time migration with source wavefield reconstruction strategy. J. Geophys. Eng. 9 (1), 69–74. https://doi.org/10.1088/1742-2132/9/1/008.
Gazdag, J., 1978. Wave equation migration with the phase-shift method. Geophysics 43 (7), 1342–1351. https://doi.org/10.1190/1.1440899.
Griewank, A., Walther, A., 1997. Treeverse: an implementation of checkpointing for the reverse or adjoint mode of computational differentiation. ACM Trans. Math Software 26, 200–223.
Gu, B., Liu, Y., Li, Z., et al., 2014. An excitation potential imaging condition for elastic reverse time migration. J. Appl. Geophys. 108, 124–139. https://doi.org/10.1016/j.jappgeo.2014.07.002.
Gu, B., Liu, Y., Ma, X., et al., 2015. A modified excitation amplitude imaging condition for prestack reverse time migration. Explor. Geophys. 46 (4), 359–370. https://doi.org/10.1071/EG14039.
Hemon, C., 1978. Equations d'onde et modeles. Geophys. Prospect. 26 (4), 790–821. https://doi.org/10.1111/j.1365-2478.1978.tb01634.x.
Hill, N.R., 2001. Prestack Gaussian-beam depth migration. Geophysics 66 (4), 1240–1250. https://doi.org/10.1190/1.1487071.
Jia, J., Zhao, Q., Xu, Z., et al., 2021. Variational bayes' method for functions with applications to some inverse problems. SIAM J. Sci. Comput. 43, A355–A383.
Jiang, B., Zhang, J., Zhang, H., et al., 2021. Fast least-squares prestack time migration via accelerating the explicit calculation of hessian matrix with dip-angle fresnel zone. Petrol. Sci. https://doi.org/10.1016/j.petsci.2021.12.017.
Keho, T.H., Beydoun, W.B., 1988. Paraxial ray Kirchhoff migration. Geophysics 53 (12), 1540–1546. https://doi.org/10.1190/1.1442435.
Kelly, K.R., Ward, R.W., Treitel, S., et al., 1976. Synthetic seismograms: a finite-difference approach. Geophysics 41 (1), 2–27. https://doi.org/10.1190/1.1440605.
Komatitsch, D., Tromp, J., 2003. A perfectly matched layer absorbing boundary condition for the second-order seismic wave equation. Geophys. J. Int. 154 (1), 146–153. https://doi.org/10.1046/j.1365-246X.2003.01950.x.
Kunisch, K., Volkwein, S., 2002. Galerkin proper orthogonal decomposition methods for a general equation in fluid dynamics. SIAM J. Numer. Anal. 40 (2), 492–515. https://doi.org/10.1137/S0036142900382612.
Li, Q., Fu, L., Wu, R., et al., 2020. Efficient acoustic reverse time migration with an attenuated and reversible random boundary. IEEE Access 8, 34598–34610. https://doi.org/10.1109/ACCESS.2020.2974862.
Li, Z., Qu, Y., 2022. Research progress on seismic imaging technology. Petrol. Sci. 19 (1), 128–146. https://www.sciencedirect.com/science/article/pii/S1995822622000218.
Liu, S., Li, X., Liu, Y., et al., 2014a. Dispersion analysis of triangle-based finite element method for acoustic and elastic wave simulations. Chin. J. Geophys. 57 (5), 712–725. https://agupubs.onlinelibrary.wiley.com/doi/abs/10.1002/cjg2.20135.
Liu, S., Li, X., Wang, W., et al., 2014b. A mixed-grid finite element method with pml absorbing boundary conditions for seismic wave modelling. J. Geophys. Eng. 11 (5), 1–13. https://doi.org/10.1088/1742-2132/11/5/055009.
Liu, S., Li, X., Wang, W., et al., 2015. Source wavefield reconstruction using a linear combination of the boundary wavefield in reverse time migration. Geophysics 80 (6), S203–S212. https://doi.org/10.1190/geo2015-0109.1.
Liu, Y., Teng, J., Liu, S., et al., 2013. Explicit finite element method with triangle meshes stored by sparse format and its perfectly matched layers absorbing boundary condition. Chin. J. Geophys. 56 (9), 3085–3099. https://doi.org/10.6038/cjg20130921.
Lu, K., Chen, Y., Cao, Q., et al., 2017. Bifurcation analysis of reduced rotor model based on nonlinear transient pod method. Int. J. Non Lin. Mech. 89, 83–92. https://doi.org/10.1016/j.ijnonlinmec.2016.11.013.
Lu, K., Jin, Y., Chen, Y., et al., 2019. Review for order reduction based on proper orthogonal decomposition and outlooks of applications in mechanical systems. Mech. Syst. Signal Process. 123, 264–297. https://doi.org/10.1016/j.ymssp.2019.01.018.
Luo, Z., Ou, Q., Wu, J., et al., 2012. A reduced FE formulation based on POD method for hyperbolic equations. Acta mathematica scientia, Series B 32 (5), 1997. http://121.43.60.238/sxwlxbB/EN/abstract/article_12051.shtml, 2009.
McMechan, G.A., 1983. Migration by extrapolation of time-dependent boundary values. Geophys. Prospect. 31 (3), 413–420. https://doi.org/10.1111/j.1365-2478.1983.tb01060.x.
Meng, W., Fu, L., 2017. Seismic wavefield simulation by a modified finite element method with a perfectly matched layer absorbing boundary. J. Geophys. Eng. 14 (4), 852–864. https://doi.org/10.1088/1742-2140/aa6b31.
Nguyen, B., McMechan, G., 2012. Excitation amplitude imaging condition for prestack reverse-time migration. Geophysics 78 (1), S37–S46. https://doi.org/10.1190/geo2012-0079.1.
Nguyen, B., Mcmechan, G., 2015. Five ways to avoid storing source wavefield snapshots in 2d elastic prestack reverse time migration. Geophysics 80 (1), S1–S18. https://doi.org/10.1190/geo2014-0014.1.
Richter, G.R., 1994. An explicit finite element method for the wave equation. Appl. Numer. Math. 16 (1), 65–80. https://doi.org/10.1016/0168-9274(94)00048-4.
Saad, Y., 2003. Iterative Methods for Sparse Linear Systems, second ed. Society for Industrial and Applied Mathematics https://epubs.siam.org/doi/abs/10.1137/1.9780898718003.
Schmidthäusler, D., Schöps, S., Clemens, M., 2013. Reduction of linear subdomains for non-linear electro-quasistatic field simulations. IEEE Trans. Magn. 49 (5), 1669–1672. https://doi.org/10.1109/TMAG.2013.2238905.
Sotelo, E., Favino, M., Gibson, R., 2020. Application of the generalized finite element method to the acoustic wave simulation in exploration seismology. Geophysics 86 (1), T61–T74. https://doi.org/10.1190/geo2020-0324.1.
Su, B., Li, H., Liu, S., et al., 2019. Modified symplectic scheme with finite element method for seismic wavefield modeling. Chin. J. Geophys. 62 (4), 1440–1452. https://doi.org/10.6038/cjg2019M0538.
Sun, W., Fu, L., 2013. Two effective approaches to reduce data storage in reverse time migration. Comput. Geosci. 56, 69–75. https://doi.org/10.1016/j.cageo.2013.03.013.
Symes, W., 2007. Reverse time migration with optimal checkpointing. Geophysics 72 (5), SM213–SM221. https://doi.org/10.1190/1.2742686.
Tan, S., Huang, L., 2014. Reducing the computer memory requirement for 3D reverse-time migration with a boundary-wavefield extrapolation method. Geophysics 79 (5), S185–S194. https://doi.org/10.1190/geo2014-0075.1.
Whitmore, N.D., 1983. Iterative Depth Migration by Backward Time Propagation. SEG Technical Program Expanded Abstracts 1983. Society of Exploration Geophysicists, pp. 382–385. https://doi.org/10.1190/1.1893867.
Yang, J., Huang, J., Wang, X., et al., 2015. An amplitude-preserved adaptive focused beam seismic migration method. Petrol. Sci. 12 (3), 417–427. https://doi.org/

10.1007/s12182-015-0044-7.
Yang, P., Brossier, R., Métivier, L., et al., 2016. Wavefield reconstruction in attenuating media: a checkpointing-assisted reverse-forward simulation method. Geophysics 81 (6), R349–R362. https://doi.org/10.1190/geo2016-0082.1.
Yao, G., Jakubowicz, H., 2016. Least-squares reverse-time migration in a matrix-based formulation. Geophys. Prospect. 64 (3), 611–621. https://doi.org/10.1111/1365-2478.12305.
Zhang, R., Huang, J., Zhuang, S., et al., 2019. Target-oriented Gaussian beam migration using a modified ray tracing scheme. Petrol. Sci. 16, 1301–1319. https://doi.org/10.1007/s12182-019-00388-y.
Zhang, Y., Sun, J., Karazincir, M., et al., 2002. Amplitude preserving v(z) pre-stack Kirchhoff migration and demigration. In: Expanded Abstract of 64th EAGE Annual Conference. Taylor & Francis, pp. 1–3. https://doi.org/10.1071/ASEG2003ab117.
Zhu, S., Dede, L., Quarteroni, A., 2016. Isogeometric analysis and proper orthogonal decomposition for the acoustic wave equation. ESAIM Math. Model. Numer. Anal. 51 (4), 1197–1221. https://doi.org/10.1051/m2an/2016056.